Title

Decoupling exchange bias and coercivity enhancement in a perovskite oxide exchange spring bilayer

Journal

Physical Review Materials, 3(1)

ISSN

2476-0455

Authors

Kane, Alexander M
Chopdekar, Rajesh V
N'Diaye, Alpha T
et al.

Publication Date

2019

DOI

10.1103/physrevmaterials.3.014413

Peer reviewed

Decoupling exchange bias and coercivity enhancement in a perovskite oxide exchange spring bilayer

Alexander M. Kane,[1] Rajesh V. Chopdekar,[2] Alpha T. N'Diaye,[2] Andreas Scholl,[2] Elke Arenholz,[2] Apurva Mehta,[3] and Yayoi Takamura[1]

[1]*Department of Materials Science and Engineering, University of California, Davis, California, USA*

[2]*Advanced Light Source, Lawrence Berkeley National Laboratory, Berkeley, California, USA*

[3]*Stanford Synchrotron Radiation Lightsource, SLAC National Accelerator Laboratory, Menlo Park, California, USA*

A wedge bilayer of epitaxial 4–8 nm $La_{0.7}Sr_{0.3}CoO_3$(LSCO)/6-nm $La_{0.7}Sr_{0.3}MnO_3$(LSMO), hard and soft ferromagnets (FM) respectively, was studied using soft x-ray magnetic spectroscopy to elucidate the interplay between the magnetic and electronic properties of the constituent layers. This system exhibits magnetic and electronic segregation within the LSCO layer characterized by soft FM Co^{2+} ions at the interface (s-LSCO), which is biased by the underlying hard LSCO layer (h-LSCO), characterized by predominantly Co^{3+}/Co^{4+} FM ions. For a 5.1-nm layer, the interfacial Co^{2+} ion concentration is maximized and the h-LSCO coercivity is minimized, while the opposite is true for a 7.8-nm LSCO layer. These dual trends in Co^{2+} ion concentration and h- LSCO coercivity within the LSCO serve to independently affect the exchange bias and coercivity of the soft FM layer, resulting in inverse trends between these properties that typically vary simultaneously.

I. INTRODUCTION

Perovskite oxide thin films are prime candidate materials for implementation in next-generation spintronic devices due to their charge, orbital, lattice, and spin degrees of freedom, and extreme sensitivity to external stimuli such as applied magnetic/electric fields [1,2] chemical doping [3], and lattice strain [4,5]. Modern advances in thin film growth techniques have enabled unit-cell precision of the layer thickness and roughness, providing a rich playground to explore the emer- gent interfacial phenomena that arise due to electronic, mag- netic, or structural reconstruction in oxide heterostructures [6–9]. One example of an interfacial interaction to find wide scale technological implementation is exchange bias (EB), which is manifested in a horizontal shift in the ferromag- netic (FM) hysteresis loop. EB has been observed in a variety of perovskite oxide systems composed of materials with differing magnetic order, ranging from the traditional— antiferromagnetic (AFM)/FM [10–12] and FM/FM multilay- ers [13–15]—to the unexpected, in AFM/paramagnetic (PM) [16] and FM/PM multilayers [17,18]. These observations are often accompanied by an interfacial modulation of the transi- tion metal valence state [13,16–18], which induces changes to the indirect exchange interactions distinct from those within the rest of the film. Furthermore, strain engineering has been shown to drive local structural changes near the substrate/film interface which results in a thin AFM layer that biases the rest of the $La_{0.7}Sr_{0.3}MnO_3$(LSMO) film [19]. Additionally, the interface between the AFM $BiFeO_3$ and LSMO was character- ized by an unexpected interfacial Fe FM layer which coupled antiferromagnetically to the LSMO layer, and thus exhibited EB. The formation of this FM Fe layer was attributed to the interplay between the orbital and spin degrees of free- dom at the bilayer interface [20]. These examples highlight

the wide variety of mechanisms by which EB is introduced and manipulated in oxide heterostructures, rendering their study intriguing from both an application and a fundamental perspective.

This work focuses on bilayers of $La_{0.7}Sr_{0.3}CoO_3$(LSCO) and LSMO, hard and soft ferromagnets, respectively. LSMO has been widely studied for use in magnetoresistive random access memory and magnetic tunnel junctions due to its colossal magnetoresistance [21], half-metallicity [22], and relatively high Curie temperature (T_C 360 K) [23]. LSCO has recently received interest due to the existence of sponta- neous magnetoelectronic phase separation (MEPS) wherein FM/metallic clusters exist within a nonmagnetic/insulating matrix [24], as well as spin state transitions which arise from the similarity between the Hund's Rule coupling and crystal field splitting energies [24]. Beyond a critical Sr doping of 0.18, the FM clusters form a percolation network that results in long-range FM/metallic behavior [24]. Previous work on LSCO/LSMO bilayers revealed the appearance of a soft FM (s-LSCO) interface layer characterized by ferro- magnetically ordered Co^{2+} ions at the LSCO/LSMO inter-
face. This s-LSCO layer, estimated to be 1–2-nm thick [25], is magnetically coupled to the soft LSMO layer such that the hard/soft magnetic interface does not coincide with the chemical interface [26]. The remainder of the LSCO layer un- derneath the s-LSCO layer retained the hard FM behavior and Co^{3+}/Co^{4+} (h-LSCO) mixed-valent states expected for bulk- like LSCO, which imposes a unidirectional anisotropy on the s-LSCO/LSMO hybrid layer and causes an EB shift similar to metallic exchange spring systems [27,28]. However, the effect of changing LSCO thickness on the nature of the magnetic interface, as well its effect on the properties of the soft FM layer, remain unexplored. In the present study, we combine the small spot size of synchrotron-based radiation techniques

with a wedge bilayer of varying LSCO thickness and constant LSMO thickness, allowing the systematic investigation of the bilayer's magnetic behavior as a function of LSCO thickness. In this way, small synthesis-to-synthesis variations can be eliminated allowing access to even subtle variation. Moreover, the constant LSMO layer ensures an equal probing depth into the LSCO layer during soft x-ray magnetic spectroscopy measurements. We observe unexpected, competing trends in soft-FM layer coercivity and EB concurrent with variation in the Co electronic/magnetic structure, demonstrating the ability to tune functional properties via Co valence state variation within the intermediary s-LSCO layer.

II. METHODS AND MATERIALS

The LSCO/LSMO wedge bilayer was deposited by pulsed laser deposition on a 10 5 mm (001)-oriented $(LaAlO_3)_{0.3}(Sr_2AlTaO_6)_{0.7}$(LSAT) substrate. By offsetting the substrate heater from the center of the plume axis, a LSCO wedge layer with thickness varying from 4–8 nm was grown using the natural gradient of the plume [29]. A uniform 6-nm LSMO layer was grown after shifting the substrate back to the plume center. Both layers were grown using a KrF (248 nm) excimer laser, with 0.9 J/cm^2 laser fluence, at 700 °C substrate temperature, 0.3 Torr O_2 pressure, and 1 Hz laser repetition rate. Samples were cooled to room temperature in 300 Torr O_2 to ensure proper oxygen stoichiometry. A single-layer LSCO wedge was also grown with the same deposition parameters to ensure any changes to the Co electronic/magnetic structure in the bilayer can be solely attributed to the FM/FM interface rather than the deposition method.

Structural characterization was performed using resonant x-ray reflectivity (RXRR) and high-resolution x-ray diffrac- tion (XRD) [ω-2θ scans and reciprocal space mapping (RSM)] at beamlines 2-1 and 7-2 of the Stanford Synchrotron Radiation Lightsource (SSRL). RXRR profiles were mea- sured at the Co and Mn *K*-edge energies to increase scattering contrast in perovskite bilayers and superlattices with similar chemical densities [30]. X-ray absorption near edge structure energy spectra were used to obtain the *K*-edge absorption peaks, after which a Kramers-Kronig transformation was per-formed to obtain the energies at which the real part of the x-ray dispersion correction factor, f', is at a minimum. At these experimentally determined energies, 7723 and 6552 eV for Co and Mn, respectively, the scattering contrast between the LSCO and LSMO layers is increased, thus allowing us to extract chemical profiles for the bilayers. An off-resonant measurement was also collected at 8000 eV, similar in energy to the Cu $K_{\alpha 1}$ x-rays used in many lab diffractometers. The ω- 2θ scans and RSMs were measured at an off-resonant 14-keV photon energy.

Element-specific magnetic/electronic characterization was performed using soft x-ray absorption (XA) and x-ray mag- netic circular dichroism (XMCD) spectroscopy at beamlines 6.3.1 and 4.0.2 of the Advanced Light Source (ALS) using two detection methods. Total electron yield (TEY) is limited by the escape length of secondary electrons (4–10 nm [31]) and while it probes the entire thickness of the LSMO layer, it is mostly sensitive to the portion of the LSCO layer at the

LSCO/LSMO interface. The luminescence yield (LY) detec- tion method provides a signal for the entire film thickness by measuring the conversion of x-ray photons transmitted through the bilayer into visible light photons by the lumines- cent substrate [32]. Through the comparison of spectra mea- sured by these two methods, the effects at the LSCO/LSMO interface can be separated from that of the LSCO layer as a whole. The XA/XMCD spectra were measured at 80 K with x-rays incident 60° from the surface normal and applied mag- netic field parallel to the x-rays. XMCD spectra were collected after field cooling from room temperature in a 0.3 T magnetic field, using alternating right and left circularly polarized light, in order to capture both s-LSCO and h-LSCO contributions to the overall signal. Soft x-ray photoemission electron mi- croscopy (X-PEEM) at beamline 11.0.1 of the ALS was used to image the FM domains by collecting images with right/left circularly polarized x-rays at energies corresponding to the peaks in XMCD spectra at the Co- and Mn-L_3 edges. An asymmetry calculation $(I_{RCP} - I_{LCP})/(I_{RCP} + I_{LCP})$ was then performed to isolate the magnetic domain contrast from topography and work function contrast. X-rays were aligned along the [001] substrate direction, and the re- sulting image contrast is proportional to the cosine of the angle between the local magnetization and x-ray helicity.

III. RESULTS

RXRR profiles were collected at six thicknesses of the LSCO layer and the datasets for all three x-ray energies at a single measurement point were fit simultaneously to one structural model using the GenX reflectivity software [33]. The measurement points for the RXRR and magnetic spectroscopy measurements were correlated by collecting the off-specular fluorescence yield of the Co/Mn ions and the TEY signal of the surface LSMO layer, respectively, across the length of the wedge. Once the edges of the wedge were determined, six measurements were taken with the same point spacing. RXRR data were fit by first allowing the LSMO and LSCO layer fit parameters to vary at all six measurement points. Subsequently, thickness, density, and roughness values of the LSMO layers and LSCO surface layer were averaged and assumed to be uniform, and then held constant in a second round of fits to isolate changes in the LSCO layer. The structural parameters of the LSCO layer extracted from the fits indicate close agreement to the targeted nominal thickness values: 7.8 nm at the thickest measurement point to 5.1 nm at the thinnest in roughly 0.5-nm steps. The interface roughness was ≤0.4 nm for all points indicating a single-unit cell smooth interface with minimal chemical intermixing. Representative Co *K*-edge RXRR profiles and fits are shown in Fig. 1 for three positions on the wedge. Detailed structural model information, including the full RXRR fit series and structural parameter tables, is provided in the Supplemental Material [34], Fig. S1 and Tables SI–SVI.

Figure S2 shows ω-2θ XRD scans around the (002) peak at the same three positions on the wedge bilayer, which have been fit using the Bruker LEPTOS software package [35] and tabulated in Table SVII. The *c/a* ratios are further compared to a bilayer of 20-nm-sublayer thicknesses [36]. Prominent

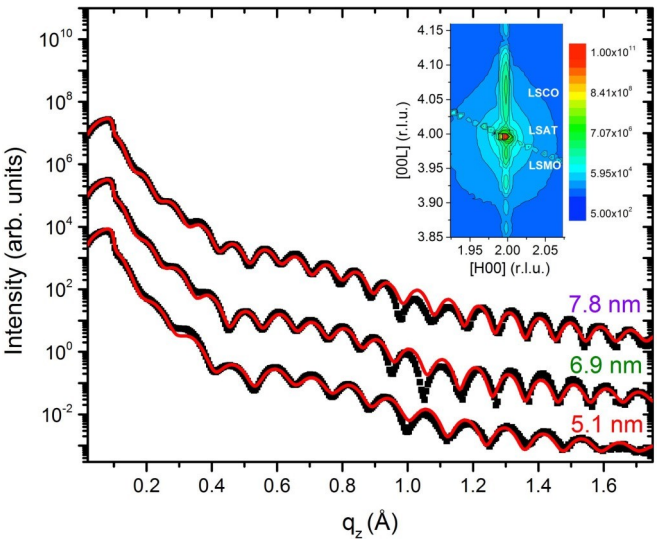

FIG. 1. Co *K*-edge RXRR profiles (black) and fits (red) at the thin, middle, and thick regions of the LSCO/LSMO wedge bilayer. Inset: An RSM around the (204) peak from the middle of the wedge bilayer.

Kiessig fringes confirm smooth interfaces and structural co- herence irrespective of position along the LSCO thickness gradient. The inset of Fig. 1 shows a representative RSM around the (204) substrate reflection from the middle of the LSCO wedge. Both the LSMO and LSCO film peaks are vertically aligned with the *H* value of the substrate, indi- cating that the in-plane lattice parameters of both layers are matched to that of the LSAT substrate. The respective lattice parameters correspond to a value of 0.7% lattice mismatch ($[a_{film} - a_{substrate}]/a_{substrate}$) for the LSMO layer [37] and 0.6% lattice mismatch for the LSCO layer [38], which are in compressive and tensile strain states, respectively. The full set of RSMs is shown in Fig. S3.

The magnetic switching behavior and relative alignment of the magnetization of the hard and soft layers at each point across the wedge bilayer were investigated using XMCD hysteresis loops, where the photon energy was tuned to the maxi- mum XMCD signal and the magnetic field was swept to trace out major and minor hysteresis loops. This technique allows for the determination of the individual magnetic switching contributions from Co and Mn ions that are unattainable via bulk magnetometry measurements. Minor XMCD hysteresis loops at the Co and Mn L_3 edge were taken at 80 K using a sweeping field of 0.15 T after a 1.8 T biasing field, such that the underlying h-LSCO layer remains positively saturated and only the soft layers of the bilayer are switched. Mn loops were taken using LY detection to increase the sensitivity of the LSMO layer closest to the chemical interface, while Co loops used TEY to emphasize detection of the Co ions nearest the LSCO/LSMO interface. Representative Mn-XMCD minor hysteresis loops plotted in Fig. 2(a) exhibit two systematic trends: a thicker underlying LSCO layer serves to *decrease* the soft layer coercivity while *increasing* its horizontal EB shift. The inverse coupling of these two properties, which typically display similar trends in EB systems [12,18,39–42], is rather unexpected and unique. Representative Co and Mn

minor hysteresis loops at the thinnest measured spot of the LSCO wedge are shown in Fig. 2(b), confirming that the s- LSCO layer switches simultaneously with the adjacent LSMO layer. Additionally, the slight drag in the s-LSCO layer switch- ing, evidenced by the increased saturating field for the Co loop relative to Mn, is likely a result of the strong exchange in- teraction at the s-LSCO/h-LSCO interface. Figure 2(c) shows how EB and coercivity can be tuned in opposite directions by adjusting the LSCO film thickness.

X-PEEM images from the center of the wedge bilayer (i.e., 6.5 nm LSCO) shown in Figs. 2(d) and 2(e) further highlight the coupling between the LSMO and s-LSCO layers. The Co images were taken at 777.9 eV, which corresponds to the Co^{2+} XMCD peak energy rather than the bulk LSCO XMCD peak at 779.1 eV. A clear one-to-one correlation be- tween the Mn/Co FM domain shape, size, and magnetization orientation is observed, indicating strong exchange coupling between the two layers via an expected Co^{2+}-Mn^{4+} superex- change interaction [43]. The size and shape of the domains is reminiscent of the domains observed in LSMO films [44]. In contrast, the micrometer-sized Co domains are significantly larger than those observed in bulk LSCO [45]. Indeed, the Co-XMCD image also exhibits subtle, spotted texturing on a 100-nm length scale, consistent with previously observed domains in LSCO films [45], and are therefore attributed to the Co^{3+}/Co^{4+} type domains in the zero-field cooled h-LSCO layer. The buried h-LSCO layer could lead to a significant reduction in the raw signal of the Co^{3+}/Co^{4+} domains with respect to the interface Co^{2+} magnetic signal, so we conclude that the lower relative contrast of the smaller h-LSCO type domains suggests that this magnetic layer is located below the s-LSCO region at the LSCO/LSMO interface.

Both the biased minor-hysteresis loops and X-PEEM im-
ages indicate strong coupling between the LSMO/s-LSCO layers, but the origin of the trends in coercivity/EB remain unclear. Because the effects of changing LSCO thickness on the LSMO magnetic behavior is mediated by the s-LSCO interface layer, Co-XA/XMCD spectroscopy was performed to elucidate its electronic/magnetic structure, and to correlate to the observed soft FM layer switching behavior. Co-XA spectra were collected in both TEY and LY detection methods to isolate the effects of the LSCO/LSMO interface from the rest of the film. These spectra were compared to reference spectra for Co^{2+} ions from a single crystal of spinel Co_2FeO_4 and mixed valent Co^{3+}/Co^{4+} ions from a 28-nm-thick LSCO film.

The Co-XA TEY spectra show an increase in the spectral features characteristic of Co^{2+} ions, denoted as features A and B in Fig. 3(a), at the thinnest end of the LSCO wedge (red). The magnitude of these features all gradually decrease
as the LSCO thickness increases, while the overall L_3 peak energy steadily shifts to higher photon energy and towards the LSCO reference peak (feature C). Due to the constant thickness of the surface LSMO layer and the limited probing depth for the TEY detection method, these measurements are expected to sample a constant depth into the LSCO layer regardless of measurement position. Previous measurements on separate bilayers were unable to clarify if Co-XA spec- tra changes were due to decreasing Co^{2+} ion concentration, varying s-LSCO layer thicknesses, a product of TEY probing

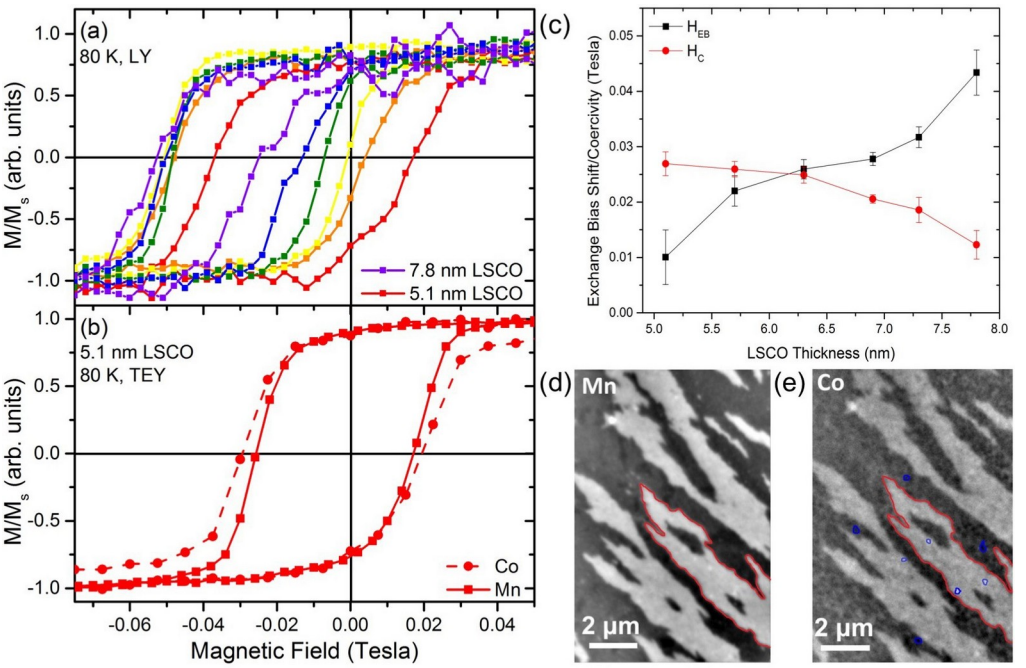

FIG. 2. (a) Minor Mn-XMCD hysteresis loops after a 1.8 T biasing field at 80 K, and (b) Co and Mn XMCD loops at 4.5-nm LSCO thickness which display simultaneous switching. LSCO thickness increases from red to purple in 0.5-nm steps. (c) Exchange bias increases, while the coercivity decreases as a function of LSCO thickness. XMCD-PEEM FM domain images acquired at the (d) Mn and (e) Co L_3 edges at 110 K. LSMO and s-LSCO Co^{2+} domains are outlined in red, with smaller h-LSCO Co^{3+}/Co^{4+} domains outlined in blue.

depth, or a combination of all three [26]. The available data suggested a model where an increase of the total LSCO thickness merely increased the h-LSCO layer thickness while the s-LSCO remained unaffected. However, the wedge bilayer data from the present study confirms that the ratio of Co^{2+} to Co^{3+}/Co^{4+} ions *decreases* with increasing LSCO thickness within the same volume of interfacial LSCO. While features A and B are largely absent from the Co-XA LY spectra in Fig. S4, there is a small 0.15-eV shift of the main peak to higher photon energy with increasing LSCO thickness, a trend which is indicative of a higher overall valence state and is consistent with the TEY measurements. The disparity between TEY spectra, which display clear Co^{2+} contributions and trends, and LY spectra, which resembles bulk LSCO for all thicknesses, further speaks to the confinement of the Co^{2+} ions to the interfacial region. The Co-XA spectra across the L_3 edge were fit using a simple linear combination of the Co^{2+} and Co^{3+}/Co^{4+} reference spectra to provide quantitative determination of the variation in Co valence states. Spectra and fits are shown in Fig. S6 and confirm a systematic decrease of Co^{2+} ion concentration as the LSCO thickness increases, from 38 2% at 5.1 nm of LSCO to 8 2% at 7.8 nm of LSCO. XA fitting weights are shown in Fig. 3(c). Figure S7 shows the Co-XA TEY spectra from multiple positions along the single-layer LSCO wedge, which exhibit no noticeable changes in line shape or peak position, confirming that the shift in Co valence is intrinsic to the bilayer rather than a change in cation composition due to the LSCO wedge layer growth procedure.

Co-XMCD TEY spectra [Fig. 3(b)] were also collected to determine the magnetic behavior of the Co ions at the interface. The maximum XMCD has been normalized to

unity so that the relative contributions from s-LSCO and h-LSCO can be compared at different measurement points across the wedge. Features D and E in Fig. 3(b) correspond to the maximum dichroism value of the s-LSCO and h-LSCO XMCD spectra, respectively. The relative intensity of feature E compared to feature D increases with increasing LSCO thickness, consistent with Fig. 3(a), which indicates an increase of h-LSCO XA features as the LSCO thickness increases.

The TEY spectra primarily capture the Co behavior at the interface, while major XMCD hysteresis loops with the LY detection method characterize the overall Co switching behavior. Major Co-XMCD hysteresis loops were collected from both the single layer LSCO wedge and wedge bilayer. While the single-layer LSCO loops in Fig. 4(a) show only one magnetic transition, the bilayer loops in Fig. 4(b) show two transitions at differing applied field values: the first transition near zero field indicates switching of the s-LSCO contribution to the total XMCD, while the second switching step is a result of the h-LSCO contribution. As evidenced by the widening of the loops in both samples, the coercivity of the hard layer increases with increasing LSCO thickness, consistent with previous studies on LSCO films grown on LSAT substrates [31]. Additionally, the relative contribution from the s-LSCO layer, signified by the initial drop in normalized magnetization at small fields, is observed to decrease with increasing LSCO
thickness. These two observations suggest a gradual decrease in the soft Co^{2+} ion magnetic contribution with increasing LSCO thickness, consistent with the Co-XA/XMCD spectra in Fig. 3.

The inverse coupling of the soft layer exchange bias and coercivity must necessarily arise from changing interactions

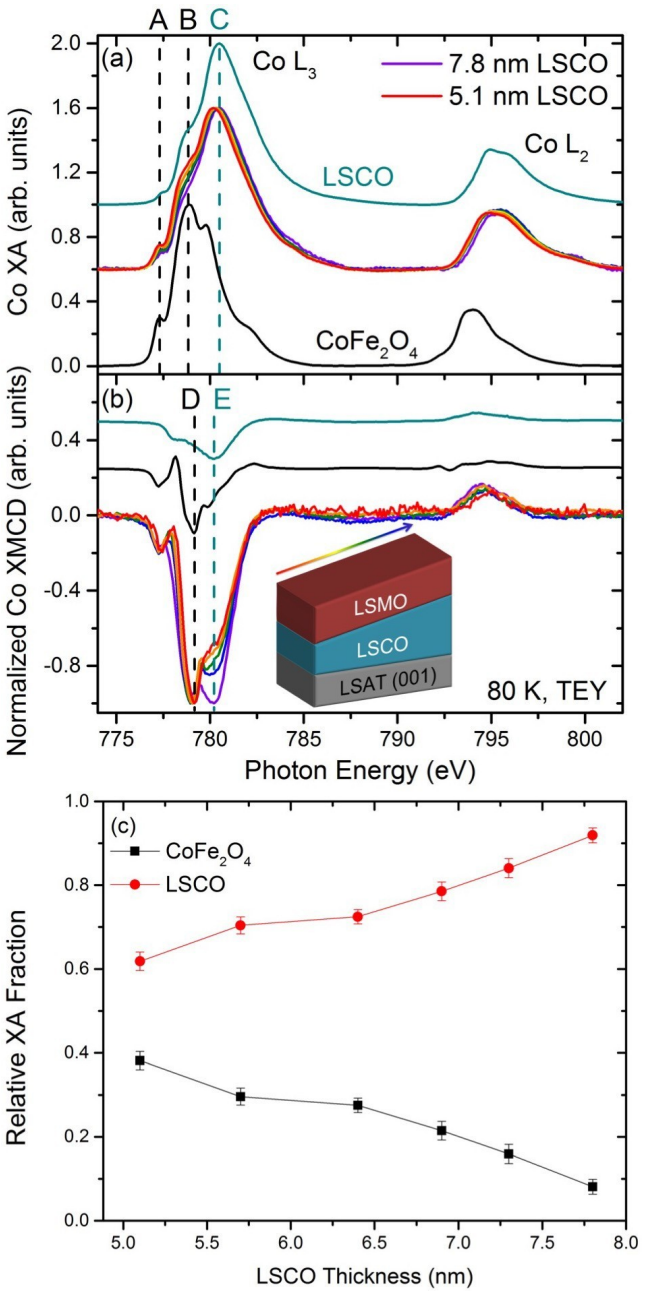

FIG. 3. (a) Co-XA spectra and (b) Co-XMCD spectra, both acquired in TEY mode. The XMCD spectra in (b) were taken after field cooling to 80 K in a 0.3-T magnetic field, and then alternating right- and left-circularly polarized light with the magnetic field fixed, such that both s-LSCO and h-LSCO contributions are captured. A, B, and D are Co^{2+} (s-LSCO) characteristic features aligned with the XA/XMCD features of the $CoFe_2O_4$ reference, while C and E are Co^{3+}/Co^{4+} mixed-valent (h-LSCO) features characteristic to pure LSCO. (c) Co-XA fraction obtained from linear combination of reference spectra. Error bars are determined via a reduced χ square analysis.

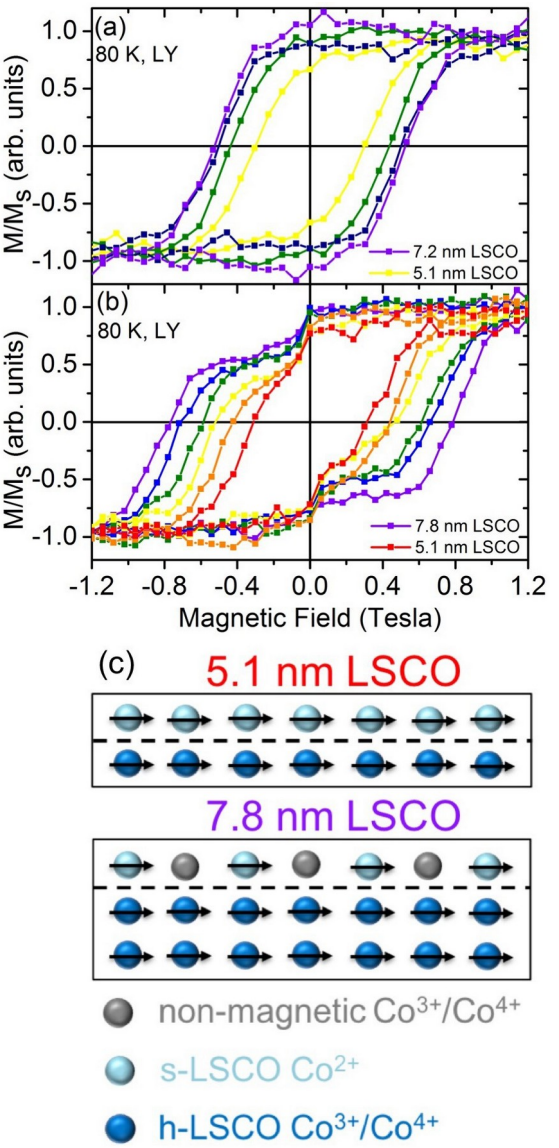

dependent on the alignment of the AFM layer's

at the hard/soft magnetic interface, which are likely related to the varying Co valence. Leighton *et al.* [46] showed that the coercivity of the FM layer in an MnF_2/Fe AFM/FM system is

FIG. 4. Major LY Co-XMCD hysteresis loops in from (a) the single layer LSCO wedge and (b) the LSCO wedge bilayer.
(c) Proposed structure of the magnetic interface between s-LSCO and h-LSCO at the two endpoints of the bilayer.

interface spins. For small cooling fields, the AFM exchange remains dominant; for large cooling fields, the AFM sur- face spins align with the cooling field and the FM layer. At these two extremes the coercivity is minimized, while the largest coercivity enhancement occurs at an intermediate cooling field that maximizes the frustration between these two opposing alignments. We present a similar argument where rather than altering the alignment of interface spins, the Co^{2+} ion concentration affects the density/strength of exchange interactions between the h-LSCO and s-LSCO layers, which allows separate trends between the EB and coercivity of the soft layer in this system.

Within this framework, one possible model that explains the inverse coupling assumes a rigid vertical separation be- tween s-LSCO and h-LSCO layers. As the LSCO thick- ness increases, the h-LSCO coercive field also increases,

which systematically increases the unidirectional anisotropy imposed by the rigid hard FM layer and gradually *increases* the exchange bias shift of the soft FM layer. At the same time, the decreasing concentration of the Co^{2+} ions in the s-LSCO interface layer results in fewer or weaker h-LSCO/s-LSCO coupling interactions. Because these interactions serve to pin the soft FM layer (consisting of the s-LSCO and LSMO layers), the decreased density of interactions would result in a *reduction* of the soft FM layer coercive field. This picture is shown schematically in Fig. 4(c).

A second possible explanation invokes the MEPS charac- teristic of LSCO where Co^{2+} ion-rich regions form clusters, such that the magnetic phase separation may occur horizontally rather than just vertically, with the s-LSCO still
weighted toward the LSCO/LSMO interface. The changes in Co-XA/XMCD spectra instead result from the differing volume fraction of these Co^{2+} ion FM clusters, and the same explanation for the trends in coercivity and EB also apply for this phase-separated interpretation; as the clusters decrease in size, the density of h-LSCO/s-LSCO interactions also de- crease. While both scenarios are plausible, the PEEM images display no clear horizontal segregation within the resolution limit (20 nm) [47] and suggest that the former is more likely of the two proposed mechanisms.

Importantly, both of these explanations require that as the Co^{2+} ion concentration at the interface decreases, they are replaced by nonmagnetic Co^{3+}/Co^{4+} ions, otherwise the number of h-LSCO/s-LSCO interactions would actually increase as the total LSCO thickness grows. Co XMCD LY spectra in Fig. S5(b) indicate a constant h-LSCO layer magnetic contribution, which would be expected to increase if the additional Co^{3+}/Co^{4+} ions were ferromagnetic. We also suggest that due to the extreme sensitivity of LSCO to Co valence and spin states [24,48,49], the introduction of Co^{2+} ions might be expected to disrupt the existence and long-range percolation of the FM Co^{3+}/Co^{4+} clusters seen in bulk LSCO. Additionally, alterations to the Co ion spin state and LSCO layer thickness is likely to produce small changes in the strain state throughout the heterostructure, which could influence the magnetocrystalline anisotropy and coercivity of the soft layer; however, any such strain changes appear to
be minimal for the thickness range studied (Table SVII), and the magnetic properties are more likely to be driven by the dynamics of the two Co magnetic layers. The MEPS in LSCO and its sensitivity to the multitude of possible valence and spin states of the Co ions highlights a unique ability to manipulate interface interactions in LSCO-based heterostructures.

IV. CONCLUSION

In summary, we have systematically studied the LSCO thickness dependence of the magnetic properties in an LSCO/LSMO wedge bilayer. Using soft x-ray magnetic spec- troscopy, we observe a gradual change to the Co electronic and magnetic structure within the s-LSCO layer which exists at the LSCO/LSMO interface; both the Co^{2+} ion concen- tration and XMCD contribution are inversely related to the LSCO thickness. Furthermore, the h-LSCO layer coercivity gradually increases with total LSCO thickness. These two phenomena combine to decouple the EB and coercivity en- hancement trends of the s-LSCO/LSMO hybrid soft FM layer. Such results highlight the unique sensitivity of charge transfer reactions at perovskite interfaces, as well as the ability to tune EB and coercivity independently via manipulating interface behavior in perovskite oxide heterostructures.

ACKNOWLEDGMENTS

Financial support for this project was provided by the Uni- versity of California, Multicampus Research Programs and Initiatives Grant No. MR-15-328528. This research is based upon work supported by the US Department of Energy (DOE), Office of Science, Office of Workforce Development for Teachers and Scientists, Office of Science Graduate Student Research (SCGSR) program. The SCGSR program is admin- istered by the Oak Ridge Institute for Science and Education (ORISE) for the DOE. ORISE is managed by ORAU under Contract No. DE-SC0014664. This research used resources of the Advanced Light Source, which is a DOE Office of Science User Facility under Contract No. DE-AC02-05CH1123. Use of the Stanford Synchrotron Radiation Lightsource, SLAC National Accelerator Laboratory, is supported by the US Department of Energy, Office of Science, Office of Basic Energy Sciences under Contract No. DE-AC02-76SF00515.

[1] A. Urushibara, Y. Moritomo, T. Arima, A. Asamitsu, G. Kido, and Y. Tokura, Phys. Rev.B **51**, 14103 (1995).

[2] S. M. Wu, S. A. Cybart, P. Yu, M. D. Rossell, J. X. Zhang,
R. Ramesh, and R. C. Dynes, Nat. Mater. **9**, 756

(2010).
[3] E. Dagotto, T. Hotta, and A. Moreo, Phys. Rep. **344**, 1 (2001).
[4] F. Yang, N. Kemik, M. D. Biegalski, H. M. Christen, E. Aren- holz, and Y. Takamura, Appl. Phys. Lett. **97**, 092503 (2010).
[5] F. Tsui, M. C. Smoak, T. K. Nath, and C. B. Eom, Appl. Phys. Lett. **76**, 2421 (2000).
[6] P. Zubko, S. Gariglio, M. Gabay, P. Ghosez, and J.-M. Triscone, Annu. Rev. Condens. Matter Phys. **2**, 141 (2011).
[7] A. Ohtomo and H. Y. Hwang, Nature (London) **427**, 423 (2004).
[8] D. A. Dikin, M. Mehta, C. W. Bark, C. M. Folkman, C. B. Eom, and V. Chandrasekhar, Phys. Rev. Lett. **107**, 056802 (2011).
[9] E. J. Moon, Q. He, S. Ghosh, B. J. Kirby, S. T. Pantelides, A. Y. Borisevich, and S. J. May, Phys. Rev. Lett. **119**, 197204 (2017).
[10] P. Padhan and W. Prellier, Phys. Rev.B **72**, 104416 (2005).
[11] P. Padhan and W. Prellier, Appl. Phys. Lett. **88**, 263114 (2006).
[12] I. Panagiotopoulos, C. Christides, N. Moutis, M. Pissas, and D. Niarchos, J. Appl. Phys. **85**, 4913 (1999).
[13] X. Ke, L. J. Belenky, C. B. Eom, and M. S. Rzchowski, Appl. Phys. Lett. **84**, 5458 (2004).
[14] X. Ke, L. J. Belenky, C. B. Eom, and M. S. Rzchowski, J. Appl. Phys. **97**, 10K115 (2005).
[15] M. Ziese, I. Vrejoiu, and D. Hesse, Appl. Phys. Lett. **97**, 052504 (2010).
[16] C. He *et al*., Phys. Rev. Lett. **109**, 197202 (2012).

[17]M. Gibert, P. Zubko, R. Scherwitzl, J. Íñiguez, and J.-M. Triscone, Nat. Mater. **11**, 195 (2012).
[18]J. C. Rojas Sánchez, B. Nelson-Cheeseman, M. Granada,
E. Arenholz, and L. B. Steren, Phys. Rev. B **85**, 094427 (2012).
[19]B. Cui, C. Song, G. Y. Wang, H. J. Mao, F. Zeng, and F. Pan, Sci. Rep. **3**, 2542 (2013).
[20] P. Yu *et al*., Phys. Rev. Lett **105**, 027201 (2010).
[21]A. P. Ramirez, J. Phys.: Condens. Matter **9**, 8171 (1997).
[22]M. Bowen, M. Bibes, A. Barthélémy, J.-P. Contour, A. Anane, Y. Lemaître, and A. Fert, Appl. Phys. Lett. **82**, 233 (2003).
[23]M. Huijben, L. W. Martin, Y.-H. Chu, M. B. Holcomb, P. Yu,
G. Rijnders, D. H. A. Blank, and R. Ramesh, Phys. Rev. B **78**, 094413 (2008).
[24]J. Wu and C. Leighton, Phys. Rev.B **67**, 174408 (2003).
[25]B. Li, R. V. Chopdekar, A. T. N'Diaye, A. Mehta, J. P. Byers, N.
D. Browning, E. Arenholz, and Y. Takamura, Appl. Phys. Lett.
109, 152401 (2016).
[26]B. Li, R.V. Chopdekar, A.T. N'Diaye, E. Arenholz, A. Mehta, and Y. Takamura, Appl. Phys. Lett. **105**, 202401 (2014).
[27]E. E. Fullerton, J. S. Jiang, M. Grimsditch, C. H. Sowers, and S. D. Bader, Phys. Rev. B **58**, 12193 (1998).
[28]E. E. Fullerton, J. S. Jiang, and S. D. Bader, J. Magn. Magn. Mater. **200**, 392 (1999).
[29]H. M. Christen and G. Eres, J. Phys.: Condens. Matter **20**, 264005 (2008).
[30]N. Kemik, M. Gu, F. Yang, C.-Y. Chang, Y. Song, M. Bibee, A. Mehta, M. D. Biegalski, H. M. Christen, N. D. Browning, and
Y. Takamura, Appl. Phys. Lett. **99**, 201908 (2011).
[31]J.-S. Lee, D. A. Arena, P. Yu, C. S. Nelson, R. Fan, C. J. Kinane,
S. Langridge, M. D. Rossell, R. Ramesh, and C.-C. Kao, Phys. Rev. Lett. **105**, 257204 (2010).
[32]A. Bianconi, D. Jackson, and K. Monahan, Phys. Rev. B **17**, 2021 (1978).
[33] M. Björk and G. Andersson, J. Appl. Crystall. **40**, 1174 (2007).
[34] See Supplemental Material at http://link.aps.org/supplemental/10.1103/PhysRevMaterials.3.014413 for additional sample characterization.
[35]*Leptos Manual* (Bruker AXS, Madison, WI, 2005).
[36]J. P. Byers, B. Li, R. V. Chopdekar, J. Ditto, D. C. Johnson,
Y. Takamura, and N. D. Browning, J. Appl. Phys. **125**, 082518 (2019)
[37]A. Vailionis, H. Boschker, W. Siemons, E. P. Houwman, D. H.
A. Blank, G. Rijnders, and G. Koster, Phys. Rev. B **83**, 064101 (2011).
[38]B. Li, R. V. Chopdekar, A. M. Kane, K. Hoke, A. T. N'Diaye,
E. Arenholz, and Y. Takamura, AIP Adv. **7**, 045003 (2017).
[39]J. Nogués and I. K. Schuller, J. Magn. Magn. Mater. **192**, 203 (1999).
[40]M. J. Carey and A. E. Berkowitz, Appl. Phys. Lett. **60**, 3060 (1992).
[41]R. D. Hempstead, S. Krongelb, and D. A. Thompson, IEEE Trans. Magn. **14**, 521 (1978).
[42]X. K. Ning, Z. J. Wang, X. G. Zhao, C. W. Shih, and Z. D. Zhang, J. Appl. Phys. **113**, 223903 (2013).
[43]R. I. Dass and J. B. Goodenough, Phys. Rev. B **67**, 014401 (2003).
[44]T. Taniuchi *et al*., Surf. Sci. **601**, 4690 (2007).
[45]V. K. Malik, C. H. Vo, E. Arenholz, A. Scholl, A. T. Young, and Y. Takamura, J. Appl. Phys. **113**, 153907 (2013).
[46]C. Leighton, J. Nogués, B. J. Jönsson-Åkerman, and I. K. Schuller, Phys. Rev. Lett. **84**, 3466 (2000).
[47]S. Anders, H. A. Padmore, R. M. Duarte, T. Renner, T. Stammler, A. Scholl, M. R. Scheinfein, J. Stöhr, L. Séve, and
B. Sinkovic, Rev. Sci. Instrum. **70**, 3973 (1999).
[48]J. B. Goodenough, J. Phys. Chem. Solids **6**, 287 (1958).
[49]M. A. Torija, M. Sharma, J. Gazquez, M. Varela, C. He,
J. Schmitt, J. A. Borchers, M. Laver, S. El-Khatib, and C. Leighton, Adv. Mater. **23**, 2711 (2011).